ACS APPLIED ENERGY MATERIALS

www.acsaem.org Article

Metal-Dependent Electrocatalytic Oxygen Reduction in Surface-Conjugated Macrocyclic Electrodes

Moumita Ghosh, Roman Ezhov, Sarah E. Braley, Yaroslav Losovyj, Gabriel Bury, Yulia N. Pushkar,* and Jeremy M. Smith*

Cite This: *ACS Appl. Energy Mater.* 2024, 7, 6717−6726 Read Online

ACCESS | Metrics & More | Article Recommendations | Supporting Information

ABSTRACT: The development of electrocatalysts for the oxygen reduction reaction (ORR) is important for building efficient fuel cells and metal−air batteries. The structures of the catalytic sites in some of the most active heterogeneous ORR catalysts are under debate. On the other hand, while molecular electrocatalysts are structurally well-defined, those that reduce O_2 tend to have limited stability and operate with a high overpotential. Here, we report metal-based graphite-conjugated electrocatalysts (GCC-MDIM; M = Fe, Co, Ni, Cu) that integrate molecularly well-defined catalyst active sites into a robust and stable heterogeneous graphite electrode. A suite of spectroscopic methods, including X-ray photoelectron spectroscopy (XPS), X-ray absorption spectroscopy (XAS), and electron paramagnetic resonance spectroscopy (EPR), has been used to confirm the structure of the catalysts. In the presence of O_2, all graphite-conjugated electrodes reveal a catalytic current, with their product selectivity dictated by the metal ion. While GCC-FeDIM shows the highest selectivity toward H_2O production, GCC-MDIM (M = Co, Ni, Cu) are selective toward H_2O_2 formation.

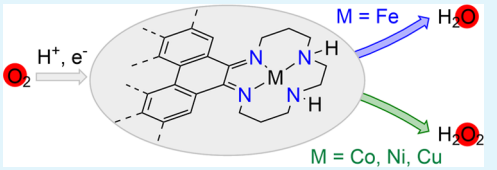

KEYWORDS: *surface-conjugated, heterogeneous, XPS, XAS, electrocatalysts, RRDE*

INTRODUCTION

Fossil fuels such as natural gas and crude oils meet the majority of the world's energy demands.[1] However, these reserves are nonrenewable and are expected to be exhausted in the coming decades. In addition, fossil fuel use is one of the major causes of air pollution and generation of the greenhouse gas CO_2, which is a major culprit in global warming.[2] This mandates the development of an alternative source of energy that is renewable, green, and sustainable.

Proton exchange membrane (PEM) fuel cells and metal−air batteries have emerged as next-generation performance energy devices for clean alternative techniques.[3] In these systems, the oxygen reduction reaction (ORR) at the cathode controls the overall performance of the system. However, the ORR is kinetically sluggish since multiple electron transfer steps are required. In PEM fuel cells, the cathodic ORR is 6 orders of magnitude slower than the anodic redox-balancing hydrogen oxidation reaction.[4−8] Therefore, research on PEM fuel cell electrocatalysts has focused on understanding and improving the efficiency of the kinetically limiting ORR half-reaction, with efforts being focused on developing effective homogeneous and heterogeneous electrocatalysts.

There are many challenges to creating high-performance ORR electrocatalysts. An ideal ORR electrocatalyst has a well-defined structure made from inexpensive materials in a reproducible synthesis, operates at low overpotential with a high rate, and has high solution stability. Current commercial electrocatalysts for the ORR are based on precious Pt metal electrodes or nanomaterials, which account for 40−50% of the cost of PEM fuel cells, limiting the large-scale application.[9−14] Nonprecious transition metal oxides have been investigated for the ORR;[15−18] however, single metal oxides have poor conductivity, requiring the use of conductive support materials for better catalytic activity.[19,20] Other heterogeneous ORR electrocatalysts include spinel-type oxides,[21−23] perovskite-type oxides,[24−26] transition metal nitrides,[27−29] transition metal phosphides,[30−33] and single-atom catalysts.[34−37] Recent work has shown that single-atom catalysts featuring first-row transition metals offer a compelling alternative to platinum and other precious metal-derived catalysts.[38−44] However, for most heterogeneous electrocatalysts, information regarding the catalytically active sites is lacking, leading to a knowledge gap that hinders the development of structure−function relationships that are useful for catalyst optimization as well as mechanistic understanding.

By contrast, the well-defined nature of homogeneous electrocatalysts provides detailed information about the active site of the catalyst. In principle, the properties of the active site can be rationally tailored for better catalyst performance. For example, metalloporphyrins have long been of interest for the ORR,[45−51] although these have typically been investigated in

Received: May 22, 2024
Revised: July 1, 2024
Accepted: July 18, 2024
Published: August 1, 2024

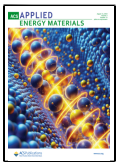

organic solvents. Building on this work, efforts have been made to incorporate such metalloporphyrins onto graphite surfaces, thereby creating heterogeneous platforms for the ORR in aqueous media.[52−55] While these electrocatalysts reduce O_2 to H_2O or H_2O_2, they require highly acidic media, have low stability, and require large overpotentials or a combination of these factors.

Recently, the Surendranath group has reported a new strategy for conjugating pyrazine units to an oxidized graphite surface.[56] This strategy can be extended to conjugate transition-metal-based macrocycles to a heterogeneous graphite surface, which provides the benefits of both homogeneous and heterogeneous electrocatalysts. We have previously adapted this strategy to integrate macrocycles into the graphite electrode to create graphite-conjugated catalysts, GCC-CoDIM and GCC-FeDIM. These electrodes have excellent catalytic performance, with the graphite-conjugated cobalt catalyst reducing nitrite to ammonia with >99% Faradaic efficiency (FE) and the graphite-conjugated iron catalyst reducing nitrate to ammonia with 88% FE,[57,58] both operating with high turnover frequencies. The graphite-conjugated catalysts (Figure 1) are well characterized and provide tunability and structural information about the catalytically active sites.

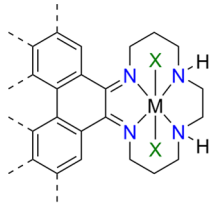

GCC-MDIM (M = Fe, Co, Ni, Cu; X = Cl, Br)

Figure 1. Structure of surface-conjugated GCC-MDIM catalysts.

Building on these developments, in this work, we investigate a series of graphite-conjugated electrodes for the electrocatalytic ORR. These electrodes share a common active site structure composed of a 3d metal ion that is coordinated to the surface-conjugated macrocyclic ligand. This work is complementary to a recent report on a series of graphite-conjugated cobalt complexes for the ORR.[59] We find that GCC-FeDIM reduces oxygen to water with high FE following a four-electron pathway, while GCC-MDIM (M = Co, Ni, and Cu) reduce oxygen to hydrogen peroxide following a two-electron pathway at neutral pH. Since GCC-MDIM are constructed by covalently attaching the metal-chelating DIM ligand to *ortho*-quinone groups that are only found at the edges of the carbon layers, we expect a similar number of active sites as observed in single-atom catalysts.[60] As characterized by their turnover frequencies (TOF), the ORR catalytic activity of our chemically modified electrodes is similar to values reported for single-atom catalysts.[60]

EXPERIMENTAL SECTION

General Considerations. All anaerobic reactions, including nonaqueous electrochemical measurements, were performed under an argon environment using standard Schlenk line techniques or in an MBraun Labmaster glovebox. Aqueous solutions were prepared using ultrapure (Type 1) water (resistivity of 18.2 MΩ·cm at 25 °C) from the Q-POD unit of a Milli-Q integral water purification system (Millipore, Billerica, MA). The pH of the solutions was measured using a Mettler Toledo pH meter at 25 °C.

Cyclic Voltammetry. The general electrochemical setup comprises three electrodes in a single-compartment cell. Unless stated otherwise, the working electrode (WE) is a 3.0 mm diameter surface-conjugated-glassy carbon disk, the reference electrode (RE) is Ag/AgCl in a 1 M KCl solution, and the counter electrode (CE) is a carbon rod electrode. A CH Instruments 720E bipotentiostat outfitted with an accompanying software suite was used for all electrochemical measurements, which were conducted under argon at room temperature. Potentials measured against the Ag/AgCl couple (1 M KCl) were converted to the reversed hydrogen electrode (RHE) by $E_{RHE} = E_{Ag/AgCl} + 0.197 + (0.059 \times pH)$. Glassy carbon disk electrodes (3 mm diameter, 0.071 cm^2) were purchased from CH Instruments. Ag/AgCl reference electrodes (1 M KCl fill solution) were purchased from CH Instruments. A rotating ring disk electrode (RRDE) was used to measure FE using RRDE-3A ver. 2.0 from RoHS compliant. The working electrode of the RRDE consists of two electrodes: (a) a 4.0 mm diameter glassy carbon disk electrode and (b) a platinum ring electrode. The counter electrode is a carbon rod, and the reference electrode is a Ag/AgCl couple in a 1 M KCl solution.

Graphite Conjugation as a Generalizable Synthetic Strategy. The graphite-conjugated catalysts $[Fe(DIM)Cl_2]^+$ and $[Co(DIM)Br_2]^+$ were prepared as previously reported.[57,58] This synthetic strategy was extended to GCC-MDIM (M = Ni, Cu), which were assembled in two discrete steps: (1) the macrocycle is assembled at the electrode and (2) metalation. The discrete cyclization and metalation steps provide a pathway for other metals and ligands to be similarly conjugated to the electrode surface. It is worth noting that attempts to create molecular analogues for Fe and Cu have been unsuccessful.[61,62]

Electrode Cleaning and Pretreatment. Glassy carbon disk electrodes were polished with a Buehler polishing pad with a 0.05 μm alumina slurry for two min, followed by rinsing with reagent-grade water. To increase the surface area and expose more quinone moieties, glassy carbon disk electrodes were anodized via controlled potential electrolysis at 3.3 V vs SCE for 10 s in 0.1 M H_2SO_4 under argon.[63] Electrodes were subsequently washed with excess reagent-grade water and methanol and dried *in vacuo* prior to conjugation and metalation. Surface functionalization was carried out by immersing preoxidized electrodes in a mixture of 1,2-bis(3-aminopropylamino)ethane (37.1 μL) and concentrated HCl (19.7 μL) in 10 mL of methanol solution, followed by 1 h stirring at room temperature.[58] The appropriate metal salts were added, and the reactions were stirred at 50 °C overnight. After cooling, electrodes were rinsed with methanol and copious amounts of water. The electrodes were soaked in 0.1 M HCl solution for 1 h to remove physisorbed and uncyclized chemisorbed linkages.

Preparation of Metal-Functionalized Monarch Carbon Powder (MDIM-Monarch). CABOT Monarch 1300 Carbon Black was obtained as a preoxidized powder. The previously reported procedure was followed to conjugate the macrocycle complex to the surface.[58] Monarch carbon (100 mg) was added to a solution of 1,2-bis(3-aminopropylamino)ethane (55.7 μL, 0.3 mmol) and 37% aqueous HCl (29.55 μL) in 15 mL of methanol. The slurry was stirred for 1 h at ambient temperature, followed by the addition of solid metal salts (0.15 mmol), and heated for 12 h at 50 °C. After 12 h, the reaction mixture was filtered, and solid black powder was rinsed with copious amounts of water and methanol. The modified carbon powder was placed in a Soxhlet extractor and extracted with hot methanol until the washings were colorless. The modified carbon powder was dried *in vacuo* and used as needed.

Preparation of GCC-MDIM-Monarch Ink. Monarch powder conjugated GCC-MDIM (M = Fe, Co, Ni, Cu) were dropcast on the disk electrode for the measurement of RRDE. To prepare the ink, 10 mg of GCC-MDIM powder, 1.8 mL of water, 0.1 mL of ethanol, and 0.1 mL of 5% Nafion were sonicated for 30 min. The ink was dropcast on a 4 mm diameter glassy carbon disk electrode and dried at 60 °C for 10 min.

X-ray Photoelectron Spectroscopy (XPS). XPS spectra were recorded for freshly prepared electrodes with no further treatment beyond the usual cleaning procedure described above. X-ray photoelectron spectra (XPS) were recorded using a Physical Electronics PHI VersaProbe II XPS with a hemispherical energy analyzer and a monochromatic aluminum Kα X-ray source (1486.6 eV). The XPS spectra were collected with an X-ray power of 25 W at 15 kV and a 100

https://doi.org/10.1021/acsaem.4c01216
ACS Appl. Energy Mater. 2024, 7, 6717−6726

μm beam size. Metallic Au, Ag, and Cu were used for instrument calibration. The PHI dual charge compensation system was used for all measurements. The ultimate VersaProbe II instrumental resolution was determined to be better than 0.125 eV using the Fermi edge of the valence band for metallic silver. XPS spectra with an energy step of 0.1 eV were recorded using *SmartSoft−XPS* v2.6.3 at pass energies of 46.95 eV for N 1s, 23.5 eV for C and O 1s, and 93.9 eV for Cl 2p, Ni 2p, and Cu 2p. All peaks were referenced to the 1s graphitic carbon peak (284.4 eV) in HOPG. The XPS spectra were processed with PHI *MultiPack* v9.3.0.3 software. Peaks were fitted using GL line shapes, *i.e.*, a combination of Gaussian and Lorentzian with 10−50% Lorentzian contents. Shirley background was used for curve fitting. The sample for XPS was placed on the sample platform using double-sided Scotch tape. Spectral reproducibility over three sample regions showed the reliability of the data. The XPS of GCC-FeDIM and GCC-CoDIM have been reported previously.[57,58]

X-ray Absorption Spectroscopy. X-ray absorption spectra were collected at the Advanced Photon Source (APS) at Argonne National Laboratory at beamline 12-BM from samples pressed into pellets in a plastic holder. The radiation was monochromatized by a Si(111) crystal. The intensity of the X-rays was monitored by three ion chambers filled with 100% nitrogen. The metal foil was placed between I_2 and I_3, and its absorption was recorded with each scan for energy calibration. The energy of the first derivative peak of the Cu, Fe, Co, and Ni metal foils was calibrated to the Cu, Fe, Co, and Ni K-edge energies of 8991.0, 7112.0, 7708.9, and 8332.8 eV correspondingly. The metal X-ray fluorescence data were collected using an X-ray fluorescence detector.

Extended X-ray absorption fine structure (EXAFS) data analysis Athena software was used for data processing.[64] Data in the energy space were pre-edge corrected, normalized, and background corrected. The processed data were converted to the photoelectron wave vector (k) space and weighted by k^3. The electron wavenumber is defined as in eq 1

$$k = [2m(E - E_0)/\hbar^2]^{1/2} \quad (1)$$

where E_0 is the threshold energy. The k-space data were truncated near zero crossings and Fourier-transformed into R-space. Artemis software was used for curve fitting. In order to fit the data, the Fourier peaks were isolated separately, or the entire experimental spectrum was fitted. The individual Fourier peaks were isolated by applying a Hanning window. Curve fitting was performed using *ab initio*-calculated phases and amplitudes from the FEFF8 program from the University of Washington. *Ab initio*-calculated phases and amplitudes were used in the EXAFS eq, eq 2[65]

$$\chi(k) = S_0^2 \sum \frac{N_j}{kR_j^2} f_{\mathrm{eff}_j}(\pi, k, R_j) e^{-2\sigma_j^2 k^2} e^{-2R_j/\lambda_j(k)} \sin(2kR_j + \varphi_{ij}(k)) \quad (2)$$

where N_j is the number of atoms in jth shell; R_j is the distance between the absorbing atoms and the atoms in jth shell; f_{eff_j} is the *ab initio* amplitude function for j, and $e^{-2\sigma_j^2 k^2}$ e^{-2} is Debye−Waller factor for shell j accounting for damping due to thermal and static disorder in the shell. The mean free path term ($e^{-2R_j/\lambda_j(k)}$) accounts for losses due to inelastic scattering. The oscillations in the EXAFS spectrum are reflected in the $\sin(2kR_j + \varphi_{ij}(k))$ term, where $\varphi_{ij}(k)$ is the *ab initio* phase function for the shell j. S_0 is an amplitude reduction factor. The EXAFS equation was used to fit experimental data using N, E_0, R, and σ^2 as variable parameters, while S_0 was kept fixed. The quality of fit was evaluated by the R-factor: if the R-factor is less than 2%, then the fit is good enough. Reduced χ^2 was used to justify the addition of new absorber-backscatter shells.

EPR Spectroscopy. X-band EPR measurements were performed on an EMX X-band spectrometer equipped with an X-band CW microwave bridge (Bruker, Billerica, MA). During EPR measurements, the sample temperature was maintained at the reported temperature by using a closed-cycle cryostat (ColdEdge Technologies, Allentown, PA). Spectrometer conditions were as follows: a microwave frequency of 9.47 GHz, a field modulation amplitude of 25 G at 100 kHz, and a microwave power of 31 mW, unless otherwise mentioned. A sample of GCC-MDIM powder was loaded into an EPR tube, and the tube was sealed with a cap.

Surface Coverage Determination from CV. Catalyst surface site density was estimated by integrating the process in the cyclic voltammogram that is attributed to the bound species. Integration was bounded by a straight line connecting the two chosen potential values. Assuming one electron transferred per [MDIM] unit, we calculated site densities using the equation $Q = nFA\Gamma_0 + Q_{\mathrm{dl}}$, where Q is the integrated charge, n is the number of electrons, F is the Faraday constant, A is the area of the electrode, Γ_0 is the surface coverage, and Q_{dl} is the double layer charge.

Surface Coverage Determination from ICP-OES. Spectra were collected using an Agilent 7850 quadrupole inductively coupled plasma-mass-spectrometry (ICP-MS). A calibration curve was generated from aqueous 2% HNO_3 containing known concentrations of Fe, Co, Ni, and Cu. Following synthesis, GCC-MDIM were cleaned with copious MeOH and water. The electrodes were scanned through a reductive potential to remove physisorbed non-macrocyclic species from the surface. The electrodes were then digested at room temperature by 200 μL of concentrated HNO_3 for 30 min, followed by dilution to 10 mL with water to create a 2% HNO_3 solution. A separate 2% HNO_3 solution was also measured as a control.

Turnover Frequency (TOF) Calculation. The TOF is defined by the equation below[66]

$$\mathrm{TOF} = \frac{j}{n \times F \times N}$$

where j (A cm^{-2}) is the current density, F (s A mol^{-1}) is the Faraday constant, and N is the site density (mol cm^{-2}).

Rotating Ring Disk Electrode (RRDE) Voltammetry and Faradaic Efficiency Calculations. The amounts of water and hydrogen peroxide produced by GCC-MDIM were calculated from rotating ring disk electrode experiments.

$$O_2 + 2H^+ + 2e^- \rightarrow H_2O_2$$

$$O_2 + 4H^+ + 4e^- \rightarrow 2H_2O$$

The rotating ring disk electrode has one glassy carbon disk and one platinum ring electrode. The GCC-MDIM (M = Fe, Co, Ni, Cu) ink was dropcast on the glassy carbon disk electrode. The potential of the disk electrode is swept from positive to negative, while the platinum ring electrode potential is held constant at 1.2 V vs RHE. During the O_2 reduction, H_2O_2 (i.e., the 2e$^-$ reduced product) produced in the working disk electrode is radially diffused to the Pt ring, where it is reoxidized to O_2. The FE of H_2O production is calculated from the ratio of the 2e$^-$/2H$^+$ current (corrected for collection efficiency) at the ring and the catalytic current at the disk. The collection efficiency (CE) of the RRDE setup is measured in a 10 mM $K_3[Fe(CN)_6]$ and 0.5 M KCl solution at a 100 mV/s scan rate and 2000 rpm rotation speed. A 36 ± 1% CE is generally observed. All of the RRDE experiments were repeated multiple times for reproducibility and showed ±10% difference in FE.

Calculation of % H_2O from RRDE.[67,68]

$$100 - \%H_2O_2 = 100 - \left(\frac{2 \times \frac{I_r}{N}}{I_d + \frac{I_r}{N}} \times 100 \right) \quad (3)$$

I_r = ring current, I_d = disk current, and N = collection efficiency.

Calculation of Electrons (n) from RRDE.

$$n = \frac{4I_d}{I_d + \frac{I_r}{N}} \quad (4)$$

I_d = disk current, I_r = ring current, and N = CE = collection efficiency.

Rotating Disk Electrode Voltammetry. The RDE measurements were recorded using the same instrument as RRDE. The GCC-MDIM

https://doi.org/10.1021/acsaem.4c01216
ACS Appl. Energy Mater. 2024, 7, 6717−6726

Scheme 1. Synthesis of GCC-MDIM (M = Fe, Co, Ni, Cu)

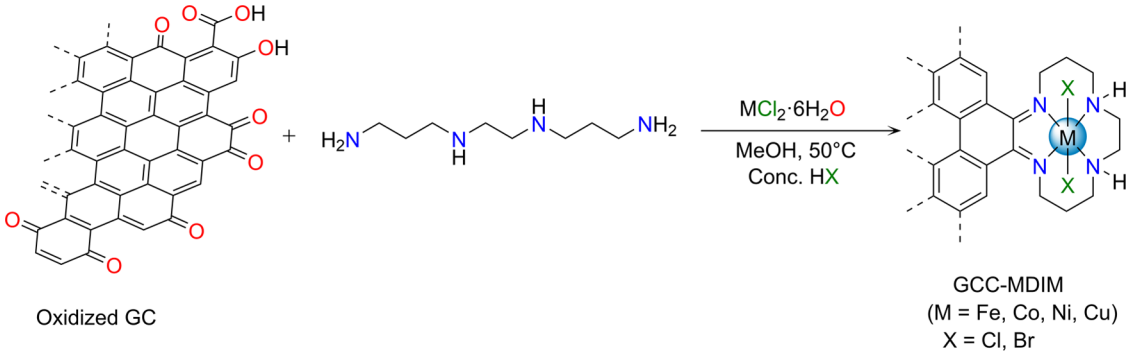

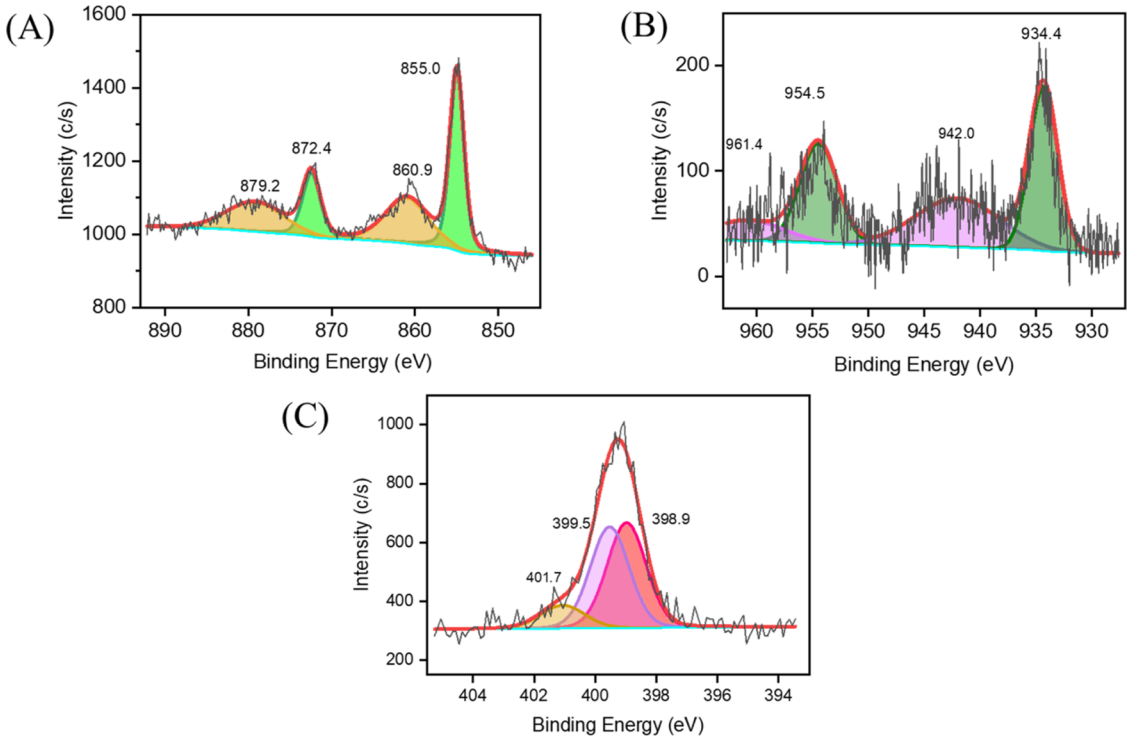

Figure 2. (A) High-resolution Ni 2p XPS spectrum of GCC-NiDIM (glassy carbon). The measured signal is in black, the fit peaks are in green and yellow, and the overall fit manifold is in red. (B) The high-resolution Cu 2p XPS spectrum of GCC-CuDIM (glassy carbon). The measured signal is in black, the fit peaks are in green and purple, and the overall fit manifold is in red. (C) The high-resolution N 1s XPS spectrum of GCC-NiDIM (glassy carbon). The measured signal is in black, the fit peaks are in red, purple, and yellow, and the overall fit manifold is in red.

ink was dropcast on the glassy carbon disk electrode. The RDE experiments were conducted by measuring linear sweep voltammetry (LSV) at a 100 mV/s scan rate at different rotation rates using Ag/AgCl (1 M KCl) reference and carbon rod auxiliary electrodes.

Calculations for the RDE Experiment. The Koutecky–Levich equation was used to calculate the number of electrons involved in the catalysis (n) and the overall rate constant of the reaction (M^{-1} s^{-1}).[55,69]

$$i_{\text{lim}}^{-1} = i_{\text{Lev}}^{-1} - i_k^{-1} \quad (5)$$

i_{lim} is the limiting current obtained from the RDE plots for O_2 reduction at the glassy carbon disk per unit area

i_{Lev} is the Levich current density = $0.62nFACD^{2/3}\upsilon^{-1/6}\omega^{1/2}$

F is the Faraday constant = 96,485 C mol^{-1}

A is the surface area of the electrode = 0.19 cm^2

C is the concentration of the O_2 in aqueous solution at pH 7 = 2.6×10^{-7} mol/mL[70]

υ is the kinematic viscosity of the solution at 22 °C = 0.01 cm^2/s^2

ω is the angular velocity of the disk = $2\pi N/60$ (in sec), where N is the linear rotation speed

D is the diffusion coefficient = 2.1×10^{-5} cm^2 s^{-1}

$j_k = nFCk_{\text{cat}}\Gamma_{\text{cat}}$

Γ_{cat} = concentration of catalyst on the surface

k_{cat} = overall rate constant of the reaction.

Tafel Data Collection. Tafel plots were obtained via potentiostatic measurements on GCC-FeDIM in a 0.1 M Na_2SO_4 electrolyte in the presence of O_2. For each run, the current produced at a specified potential after 20 s of polarization was measured. Data were collected in 20 mV increments between 0.55 V vs RHE and 0.25 V vs RHE in 0.1 M Na_2SO_4 solution. Data were collected in succession for each potential step without an intervening pause. The Tafel plots were then normalized for the number of Fe surface sites, as measured by cyclic voltammetry.

RESULT AND DISCUSSION

Synthesis and Characterization of GCC-MDIM (M = Fe, Co, Ni, Cu). The procedures previously reported for the synthesis of GCC-FeDIM and GCC-CoDIM catalysts[57,58] are readily extended to create their nickel and copper congeners. In

https://doi.org/10.1021/acsaem.4c01216
ACS Appl. Energy Mater. 2024, 7, 6717−6726

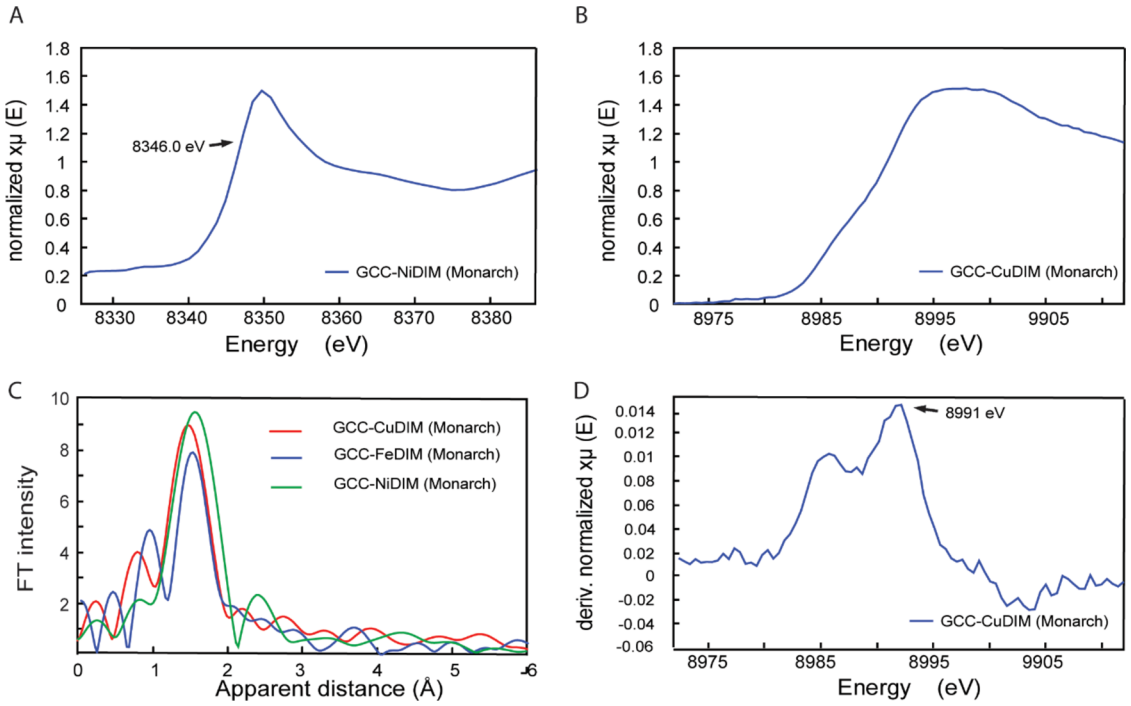

Figure 3. K-edge XANES of (A) Ni and (B) Cu. (C) The comparative figure of Cu, Fe, and Ni EXAFS indicating the presence of similar backscattering peaks. (D) The first derivative of Cu XANES indicates Cu(II) as the metal center for GCC-CuDIM on Monarch carbon.

brief, graphite electrodes are anodically treated to increase the concentration of quinone functionalities on the surface, which are then condensed with 1,2-bis(3-aminopropylamino)ethane under acidic conditions, followed by metalation in methanol (Scheme 1). Physisorbed species are removed by washing with 0.1 M HCl solution. While this synthetic strategy allows the selection of graphite-conjugated macrocycle catalysts to be systematically extended to nickel and copper, attempts toward the synthesis of both chromium and manganese catalysts were complicated by the physisorption of metal salts on the electrode surface. It is worth noting that GCC-MDIM are readily accessible via a one-pot synthetic procedure, in contrast to the synthesis of some single-atom catalysts.[39,40,60]

X-ray photoelectron spectroscopy (XPS) of the GCC-NiDIM and GCC-CuDIM electrodes confirms that the respective metal ions are incorporated onto the electrode surface. Importantly, these elements are not observed in unmodified electrodes. In the case of GCC-NiDIM, high-resolution Ni 2p XPS exhibits $2p_{3/2}$ and $2p_{1/2}$ peaks at 855.0 and 872.4 eV, respectively (Figure 2A), consistent with Ni(II).[71] The N 1s spectra can be deconvoluted into two peaks centered at 398.9 and 399.5 eV, corresponding to the imine and amine nitrogens (Figure 2C). The peak at 401.7 eV corresponds to adventitious ammonium groups, as we have previously reported.[57,58] The Ni/N ratio (1:5.4) in the survey spectrum is consistent with the proposed structural formulation. Similar N 1s spectra are observed for GCC-CuDIM. In this case, the high-resolution Cu 2p XPS spectrum of GCC-CuDIM shows $2p_{3/2}$ and $2p_{1/2}$ peaks at 934.4 and 954.5 eV, as well as the presence of shakeups, indicating the +2 oxidation state (Figure 2B).[71,72]

X-ray absorption spectroscopy (XAS) was used to evaluate the oxidation state and coordination environment of the metal center. The parameters for GCC-FeDIM[58] and GCC-CoDIM[57] were reported earlier, with the Fe and Co K-edge XANES and EXAFS confirming the formation of Fe(III) and Co(III) complexes in an octahedral coordination environment, respectively.

The Ni K-edge XANES of GCC-NiDIM has a shape that is similar to those reported for octahedral Ni(II) coordination compounds, with the first derivative at 8346.0 eV indicative of the Ni(II) oxidation state (Figure 3A).[73] The Cu K-edge XANES of GCC-CuDIM indicate the Cu(II) oxidation state of the metal center with the maximum of the XANES first derivative at 8991 eV, similar to copper(II) oxide (Figure 3B).[74] The Ni and Cu EXAFS of GCC-NiDIM and GCC-CuDIM indicate the presence of similar backscattering peaks at an apparent distance of ∼1.6 Å, corresponding to the M−N coordination sphere (Figures 3C, S7; Tables S1, S2). This is consistent with our observations for GCC-FeDIM.

EPR spectroscopy provides further evidence for the presence of Cu(II) in GCC-CuDIM. Specifically, the cryogenic (10 K) X-Band EPR spectrum reveals a paramagnetic Cu(II) feature near $g = 2$, which is similar to the spectra reported for other Cu^{2+} ions in a N4 environment (Figure S8).[75,76]

Electrochemical Properties of GCC-MDIM. We previously reported the electrochemical properties of GCC-FeDIM and GCC-CoDIM, which show surface-based redox processes at 0.33 and 0.09 V vs RHE in aqueous solution, respectively.[57,58] The CVs of GCC-NiDIM and GCC-CuDIM also show broad Gaussian-shaped redox processes at 0.17 V vs RHE (Figure S3) and 0.21 V vs RHE (Figure S5), respectively. The linear dependence of the peak current on the scan rate is consistent with a heterogeneous electrochemical process (Figures S4 and S6), which is further supported by the small peak-to-peak separation.

Electrocatalysis of GCC-MDIM. The CV of GCC-FeDIM collected in an O_2-saturated solution shows an irreversible catalytic current with an onset potential between 0.5 and 0.4 V vs RHE in aqueous solution (pH 6.0) (Figure 4). The limiting current is observed at 0.23 V vs RHE, and the current density

https://doi.org/10.1021/acsaem.4c01216
ACS Appl. Energy Mater. 2024, 7, 6717−6726

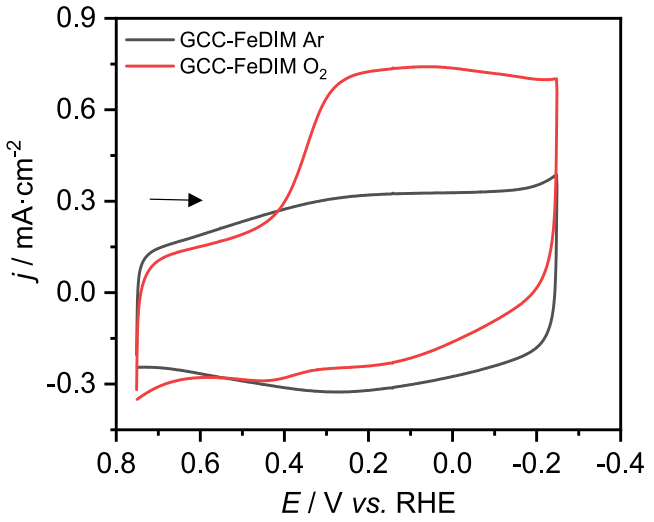

Figure 4. Cyclic voltammograms of GCC-FeDIM (glassy carbon) recorded in 0.1 M Na_2SO_4 solution (black), with O_2 (red), pH 6.0, and a scan rate of 25 mV/s.

does not significantly decrease over three repeated sweeps in the CV (Figure S10). When the electrode was polished and reimmersed in the same solution, a similar catalytic current in the presence of O_2 was not observed (Figure S11), indicating that GCC-FeDIM reduces O_2. Similarly, the catalysts GCC-MDIM (M = Co, Ni, and Cu) show a catalytic current in the presence of O_2, with all of the onset potentials between 0.5 and 0.4 V vs RHE (Figures S12–S17).

Rotating ring disk electrode (RRDE) experiments were used to benchmark the selectivity of the heterogeneous ORR by GCC-MDIM. Here, the catalysts are conjugated to high-surface-area Monarch powder that is dropcast onto a GC disk electrode using Nafion as an adhesive. Importantly, these electrodes show electrocatalytic responses similar to those observed for the glassy carbon-conjugated catalysts. Note that addition of Nafion changes the spectroscopic Fe XAS data in a single site Fe-N-C catalyst, which was interpreted as a stron catalyst ionomer interaction and Fe binding to the Nafion.[77] An unmodified Pt ring electrode with its potential fixed at 1.2 V vs RHE was used to reoxidize all of the reduced products (except water) to O_2. The current detected during the oxidation of the reactive species allows the selectivity for $4e^-/4H^+$ versus $2e^-/2H^+$ reduction to be evaluated.

These RRDE experiments used low concentrations of conjugated catalysts to maintain pseudo-first-order conditions with respect to dissolved O_2. The small difference in onset potentials (<50 mV) between the glassy carbon and RRDE disk electrodes is attributed to the fact that the Nafion adhesive prevents all of the catalysts from being directly conjugated to the electrode surface.[78]

The number of electrons involved in O_2 reduction using GCC-MDIM is calculated from eq 3 where I_d and I_r are the limiting currents obtained from the GC disk and Pt ring electrodes, respectively, and N is the collection efficiency of the electrode (0.36; see Supporting Information and Figure S26). At pH 6.0 and applied potential of 0.3 V vs RHE, only GCC-FeDIM shows selectivity for H_2O formation (n = 3.62), whereas the data for GCC-CoDIM (n = 2.71), GCC-NiDIM (n = 2.76), and GCC-CuDIM (n = 2.68) indicate selectivity toward H_2O_2. It is interesting to note that n at first decreases with increasing overpotential, but with larger overpotentials, it increases. For example, the lowest n value for GCC-FeDIM is observed at 0.18 V vs RHE (n = 3.43), whereas for GCC-CoDIM, GCC-NiDIM, and GCC-CuDIM, the lowest n value is at 0.27 V (n = 2.68), 0.26 V (n = 2.70), and 0.25 V (n = 2.65) vs RHE, respectively. We suggest that this behavior stems from the relative abilities of the metal ions to adsorb O_2.[79]

The FE for H_2O was calculated at different rotation rates by using eq 4.

Consistent with our observations above, at pH 6.0, GCC-FeDIM has the highest selectivity toward H_2O, and GCC-MDIM (M = Co, Ni, and Cu) have the highest selectivity toward H_2O_2. For example, at 0.3 V vs RHE, GCC-FeDIM has a 73% FE for H_2O, whereas GCC-CoDIM has a 42% FE for H_2O and 58% FE for hydrogen peroxide (rotation rate 2000 rpm). With GCC-CoDIM, the FE of H_2O_2 increases with changing potential to 62% at 0.26 V vs RHE. Under identical conditions, GCC-NiDIM (40% FE for H_2O and 60% FE for H_2O_2) and GCC-CuDIM (36% FE for H_2O and 64% FE for H_2O_2) show high selectivity toward H_2O_2 (Figure 5).

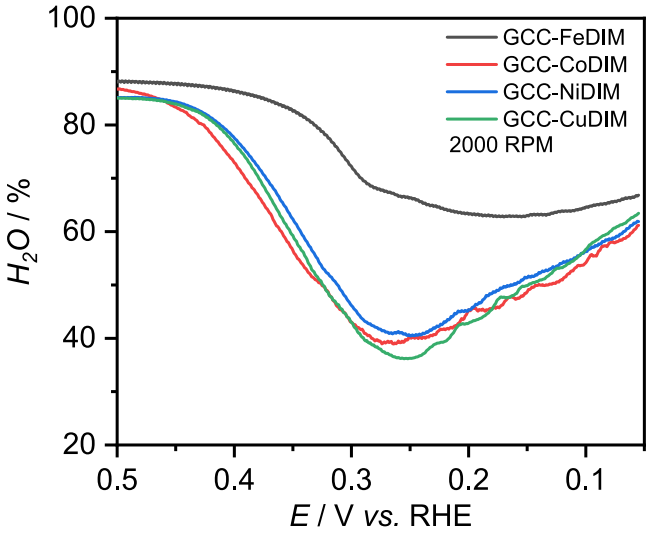

Figure 5. Comparison of Faradaic efficiency of GCC-MDIM (M = Fe, Co, Ni, and Cu) recorded in 0.1 M Na_2SO_4, pH 6.0, a scan rate of 100 mV/s, and a rotation rate of 2000 rpm. The reported Faradaic efficiencies are the average of three RRDE experiments.

We briefly note the high selectivity of GCC-MDIM (M = Co, Ni, Cu) for the formation of H_2O_2. The energy and environmental impact of the anthraquinone process for H_2O_2 production[80−82] has spurred an interest in the development of alternative electrochemical methods for H_2O_2 synthesis. While the selectivity of GCC-CoDIM for H_2O_2 at 0.1 V vs RHE is less than that reported for a Co−N−C single-atom catalyst, those of GCC-NiDIM and GCC-CuDIM are greater than the Ni−N−C (52%) and Cu−N−C (36%) analogues.[83] In addition, GCC-CoDIM shows higher FE for H_2O_2 compared to similar graphite-conjugated CB-pda-Co and CB-salophen-Co (~20%) catalysts.[59]

Previous studies on the ORR using M−N−C single-atom catalysts have shown that the catalytic activity is influenced by both the metal ion and its chemical environment.[60,83−86] A combined experimental and computational study for a series of M−N−C single atoms revealed that the selectivity could largely be attributed to the binding free energy for the HO* intermediate (* denotes active site). The largest binding free

https://doi.org/10.1021/acsaem.4c01216
ACS Appl. Energy Mater. 2024, 7, 6717−6726

energies were observed for M = Mn and Fe, which are selective for the four-electron reduction to H_2O. The highest selectivity of M = Co for H_2O_2 production is attributed to its binding free energy being most favorable for the two-electron pathway.[83] The similar structure/selectivity trend for GCC-MDIM suggests that these catalysts follow a mechanism similar to that for these M−N−C single-atom catalysts.

Under basic conditions (pH 12.9), analogous RRDE experiments reveal that the product selectivity shifts from H_2O to H_2O_2 for all GCC-MDIM electrocatalysts. This is likely due to the lower proton concentration, which influences the stability of oxygen-derived intermediates through hydrogen bonding.[70,87,88] In addition, lower proton concentrations will decrease the rate of proton transfer to these intermediates, disfavoring the formation of H_2O. Unfortunately, we are unable to evaluate the catalytic activity of these graphite-conjugated electrodes under acidic conditions, as they are not stable below pH 4.0.

The catalytic activity of GCC-FeDIM can be compared with that of Pt/C deposited on a glassy carbon. At pH 6.0, the onset potential for Pt/C is 220 mV less cathodic than that for GCC-FeDIM (Figure S24), with a greater FE for the formation of H_2O (>90 vs ∼73% for GCC-FeDIM). At pH 12.9, the difference in the onset potentials decreases to only 70 mV; however, the FE of H_2O production for GCC-FeDIM decreases (Figure S25), whereas that for Pt/C is unchanged (>90%). Nonetheless, it is interesting to note that GCC-FeDIM shows a similar onset potential to Pt/C at higher pH.

Koutecky−Levich Plots and ORR Kinetics. The selectivity and kinetics of O_2 reduction were further investigated through rotating disk electrode (RDE) experiments, where each of the GCC-MDIM catalysts was deposited on a GC disk electrode. Koutecky−Levich (K−L) plots, i_{lim}^{-1} vs $\omega^{-1/2}$, where i_{lim} is the limiting current obtained at a given angular rotation rate (ω), were generated from the current and potential curves for all four GCC-MDIM catalysts at varied rotation rates (see Figures S30−S37). The linear fit of the K−L plot provides information about the number of electrons transferred from the slope and the catalytic rate constant, k_{cat}, from the intercept. In the case of GCC-FeDIM, the number of electrons extracted from the slope of the K−L plot is found to be 3.16 at 0.2 V vs RHE, supporting a $4e^-$ reduction of O_2 to H_2O (Figure 6). This value is also in excellent agreement with the calculated RRDE value (n = 3.44; Table S3). The catalytic rate constant for GCC-FeDIM is 1.48×10^5 M^{-1} s^{-1}. A similar analysis for the other three GCC-MDIM electrocatalysts also supports the $4e^-$ reduction of O_2, with similar k_{cat} (Table S3), in contrast to the RRDE results. To evaluate the intrinsic activity of GCC-MDIM catalysts, we have estimated turnover frequencies (TOFs) based on the surface metal site density. The TOF values for GCC-MDIM are similar to those observed for Fe−N−C type single-atom catalysts,[60] likely due to their site densities being lower than for molecular electrocatalysts. It is worth noting that all GCC-MDIM are stable for over an hour during CPE, with no decrease in current observed (Figure S40).

We also conducted a Tafel analysis for GCC-FeDIM, which shows the best electrocatalytic performance for water production. Steady-state currents were normalized to the surface concentration of Fe as determined by the surface process integration in the cyclic voltammogram after multiple cycles. The resulting Tafel plot (Figure S38) is linear over the ∼0.2 V potential range with a slope of 98 mV/decade, indicating catalysis controlled by rate-limiting electron transfer. The ideal slope for a rate-limiting electron transfer is 120 mV/dec.[89,90] The nonideal value for the Tafel slope may be due to a nonideal symmetry coefficient ($\alpha \neq 0.5$) as a result of catalyst conjugation to the electrode.[91]

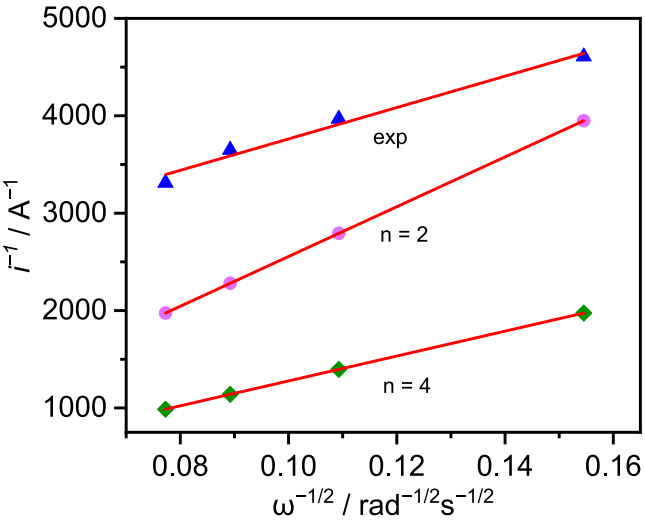

Figure 6. Koutecky−Levich (K−L) plots for GCC-FeDIM deposited onto a rotating glassy carbon disk electrode with the limiting currents observed at 0.2 V vs RHE (blue), and the theoretical K−L plots for $2e^-$ (pink) and $4e^-$ (green) processes shown for comparison. The experimental plot is the number of electrons involved in the ORR process estimated from the slope of the K−L plot for GCC-FeDIM. The R^2 values for the linear fits are 0.998 (experimental n, blue), 1.00 (theoretical n = 2, pink), and 1.00 (theoretical n = 4, green).

CONCLUSIONS

In conclusion, we report a series of heterogeneous electrodes that are constructed from earth-abundant macrocyclic complexes conjugated to a robust graphite electrode. Spectroscopic characterization of these electrodes reveals that metal ions are in a MN_4X_2 (M = Fe, Co, Ni, Cu; X = Cl, Br) coordination environment. Electrochemical experiments show that all of the electrodes are active for the ORR. Interestingly, the catalytic efficiency and product selectivity of these surface-conjugated electrodes are dependent on the identity of the metal at the active site. RRDE experiments reveal that GCC-FeDIM reduces O_2 to H_2O with higher FE, whereas GCC-MDIM (M = Co, Ni, and Cu) reduce O_2 to H_2O_2 with higher FE. These results are supported by RDE experiments.

Finally, the synthetic flexibility afforded to this catalyst framework leads us to anticipate that it can be expanded to other metal ions and ligand designs. Combined with the robustness of the catalyst, we anticipate that it has promise for multiple electrocatalytic reactions.

ASSOCIATED CONTENT

Supporting Information

The Supporting Information is available free of charge at https://pubs.acs.org/doi/10.1021/acsaem.4c01216.

All cyclic voltammetry (CVs); cathodic current vs scan rate plot; LSVs; RRDE data; FE for H_2O and H_2O_2; RDE data; Koutecky−Levich plot; Tafel plot; TOF vs potential plot; stability data; structural parameters of EXAFS fit, and site density (PDF)

https://doi.org/10.1021/acsaem.4c01216
ACS Appl. Energy Mater. 2024, 7, 6717−6726

AUTHOR INFORMATION

Corresponding Authors

Yulia N. Pushkar − *Department of Physics, Purdue University, West Lafayette, Indiana 47907, United States;* orcid.org/0000-0001-7949-6472; Email: ypushkar@purdue.edu

Jeremy M. Smith − *Department of Chemistry, Indiana University, Bloomington, Indiana 47405, United States;* orcid.org/0000-0002-3206-4725; Email: smith962@indiana.edu

Authors

Moumita Ghosh − *Department of Chemistry, Indiana University, Bloomington, Indiana 47405, United States*

Roman Ezhov − *Department of Physics, Purdue University, West Lafayette, Indiana 47907, United States;* orcid.org/0000-0001-6806-4033

Sarah E. Braley − *Department of Chemistry, Indiana University, Bloomington, Indiana 47405, United States*

Yaroslav Losovyj − *Department of Chemistry, Indiana University, Bloomington, Indiana 47405, United States*

Gabriel Bury − *Department of Physics, Purdue University, West Lafayette, Indiana 47907, United States*

Complete contact information is available at: https://pubs.acs.org/10.1021/acsaem.4c01216

Notes

The authors declare no competing financial interest.

ACKNOWLEDGMENTS

This research was supported by the NSF (CHE-2102440 to Y.N.P., CHE-2102442 to J.M.S.) and by GM132024 (T32 Molecular Biophysics Training Program to G.B.) from the National Institute of General Medical Sciences (NIGMS). The use of the Advanced Photon Source, an Office of Science User Facility operated by the U.S. Department of Energy (DOE) Office of Science by Argonne National Laboratory, was supported by the U.S. DOE under Contract DE-AC02-06CH11357. The authors thank Nikita Gupta for assistance with collecting XAS data on a Ni-based system using the CHESS synchrotron facility. Access to EPR was provided by the Amy Instrumentation Facility at Purdue University, Department of Chemistry, under the supervision of Dr. Michael Everly.

REFERENCES

(1) Shafiee, S.; Topal, E. When will fossil fuel reserves be diminished? *Energy Policy* **2009**, *37*, 181−189.

(2) Lashof, D. A.; Ahuja, D. R. Relative contributions of greenhouse gas emissions to global warming. *Nature* **1990**, *344*, 529−531.

(3) Li, Y.; Li, Q.; Wang, H.; Zhang, L.; Wilkinson, D. P.; Zhang, J. Recent Progresses in Oxygen Reduction Reaction Electrocatalysts for Electrochemical Energy Applications. *Electrochem. Energy Rev.* **2019**, *2*, 518−538.

(4) Li, J.; Zhang, Y.; Zhang, X.; Huang, J.; Han, J.; Zhang, Z.; Han, X.; Xu, P.; Song, B. S, N Dual-Doped Graphene-like Carbon Nanosheets as Efficient Oxygen Reduction Reaction Electrocatalysts. *ACS Appl. Mater. Interfaces* **2017**, *9*, 398−405.

(5) Kim, H. W.; Bukas, V. J.; Park, H.; Park, S.; Diederichsen, K. M.; Lim, J.; Cho, Y. H.; Kim, J.; Kim, W.; Han, T. H.; Voss, J.; Luntz, A. C.; McCloskey, B. D. Mechanisms of Two-Electron and Four-Electron Electrochemical Oxygen Reduction Reactions at Nitrogen-Doped Reduced Graphene Oxide. *ACS Catal.* **2020**, *10*, 852−863.

(6) Bing, Y.; Liu, H.; Zhang, L.; Ghosh, D.; Zhang, J. Nanostructured Pt-alloy electrocatalysts for PEM fuel cell oxygen reduction reaction. *Chem. Soc. Rev.* **2010**, *39*, 2184−2202.

(7) Ma, R.; Lin, G.; Zhou, Y.; Liu, Q.; Zhang, T.; Shan, G.; Yang, M.; Wang, J. A review of oxygen reduction mechanisms for metal-free carbon-based electrocatalysts. *npj Comput. Mater.* **2019**, *5*, No. 78.

(8) Gasteiger, H. A.; Kocha, S. S.; Sompalli, B.; Wagner, F. T. Activity benchmarks and requirements for Pt, Pt-alloy, and non-Pt oxygen reduction catalysts for PEMFCs. *Appl. Catal., B* **2005**, *56*, 9−35.

(9) Guo, S.; Sun, S. FePt Nanoparticles Assembled on Graphene as Enhanced Catalyst for Oxygen Reduction Reaction. *J. Am. Chem. Soc.* **2012**, *134*, 2492−2495.

(10) Jaouen, F.; Proietti, E.; Lefèvre, M.; Chenitz, R.; Dodelet, J.-P.; Wu, G.; Chung, H. T.; Johnston, C. M.; Zelenay, P. Recent advances in non-precious metal catalysis for oxygen-reduction reaction in polymer electrolyte fuel cells. *Energy Environ. Sci.* **2011**, *4*, 114−130.

(11) Raciti, D.; Kubal, J.; Ma, C.; Barclay, M.; Gonzalez, M.; Chi, M.; Greeley, J.; More, K. L.; Wang, C. Pt_3Re alloy nanoparticles as electrocatalysts for the oxygen reduction reaction. *Nano Energy* **2016**, *20*, 202−211.

(12) Wang, X.; Li, Z.; Qu, Y.; Yuan, T.; Wang, W.; Wu, Y.; Li, Y. Review of Metal Catalysts for Oxygen Reduction Reaction: From Nanoscale Engineering to Atomic Design. *Chem* **2019**, *5*, 1486−1511.

(13) Lima, F. H. B.; Zhang, J.; Shao, M. H.; Sasaki, K.; Vukmirovic, M. B.; Ticianelli, E. A.; Adzic, R. R. Catalytic Activity−d-Band Center Correlation for the O_2 Reduction Reaction on Platinum in Alkaline Solutions. *J. Phys. Chem. C* **2007**, *111*, 404−410.

(14) Cheng, F.; Chen, J. Metal−air batteries: from oxygen reduction electrochemistry to cathode catalysts. *Chem. Soc. Rev.* **2012**, *41*, 2172−2192.

(15) Cheng, F.; Su, Y.; Liang, J.; Tao, Z.; Chen, J. MnO_2-Based Nanostructures as Catalysts for Electrochemical Oxygen Reduction in Alkaline Media. *Chem. Mater.* **2010**, *22*, 898−905.

(16) Zeng, Z.; Zhang, W.; Liu, Y.; Lu, P.; Wei, J. Uniformly electrodeposited α-MnO_2 film on super-aligned electrospun carbon nanofibers for a bifunctional catalyst design in oxygen reduction reaction. *Electrochim. Acta* **2017**, *256*, 232−240.

(17) Xu, J.; Gao, P.; Zhao, T. S. Non-precious Co_3O_4 nano-rod electrocatalyst for oxygen reduction reaction in anion-exchange membrane fuel cells. *Energy Environ. Sci.* **2012**, *5*, 5333−5339.

(18) Osgood, H.; Devaguptapu, S. V.; Xu, H.; Cho, J.; Wu, G. Transition metal (Fe, Co, Ni, and Mn) oxides for oxygen reduction and evolution bifunctional catalysts in alkaline media. *Nano Today* **2016**, *11*, 601−625.

(19) Tong, Y.; Chen, P.; Zhou, T.; Xu, K.; Chu, W.; Wu, C.; Xie, Y. A Bifunctional Hybrid Electrocatalyst for Oxygen Reduction and Evolution: Cobalt Oxide Nanoparticles Strongly Coupled to B,N-Decorated Graphene. *Angew. Chem., Int. Ed.* **2017**, *56*, 7121−7125.

(20) Wu, Z.-S.; Yang, S.; Sun, Y.; Parvez, K.; Feng, X.; Müllen, K. 3D Nitrogen-Doped Graphene Aerogel-Supported Fe_3O_4 Nanoparticles as Efficient Electrocatalysts for the Oxygen Reduction Reaction. *J. Am. Chem. Soc.* **2012**, *134*, 9082−9085.

(21) Wei, C.; Feng, Z.; Scherer, G. G.; Barber, J.; Shao-Horn, Y.; Xu, Z. J. Cations in Octahedral Sites: A Descriptor for Oxygen Electrocatalysis on Transition-Metal Spinels. *Adv. Mater.* **2017**, *29*, No. 1606800.

(22) Pletcher, D.; Li, X.; Price, S. W. T.; Russell, A. E.; Sönmez, T.; Thompson, S. J. Comparison of the Spinels Co_3O_4 and $NiCo_2O_4$ as Bifunctional Oxygen Catalysts in Alkaline Media. *Electrochim. Acta* **2016**, *188*, 286−293.

(23) Wu, G.; Wang, J.; Ding, W.; Nie, Y.; Li, L.; Qi, X.; Chen, S.; Wei, Z. A Strategy to Promote the Electrocatalytic Activity of Spinels for Oxygen Reduction by Structure Reversal. *Angew. Chem., Int. Ed.* **2016**, *55*, 1340−1344.

(24) Jun, A.; Kim, J.; Shin, J.; Kim, G. Perovskite as a Cathode Material: A Review of its Role in Solid-Oxide Fuel Cell Technology. *ChemElectroChem* **2016**, *3*, 511−530.

(25) Peña, M. A.; Fierro, J. L. G. Chemical Structures and Performance of Perovskite Oxides. *Chem. Rev.* **2001**, *101*, 1981−2018.

(26) Suntivich, J.; Gasteiger, H. A.; Yabuuchi, N.; Nakanishi, H.; Goodenough, J. B.; Shao-Horn, Y. Design principles for oxygen-

reduction activity on perovskite oxide catalysts for fuel cells and metal−air batteries. *Nat. Chem.* **2011**, *3*, 546−550.
(27) Mazza, F.; Trassatti, S. Tungsten, Titanium, and Tantalum Carbides and Titanium Nitrides as Electrodes in Redox Systems. *J. Electrochem. Soc.* **1963**, *110*, No. 847.
(28) Zhong, H.; Zhang, H.; Liu, G.; Liang, Y.; Hu, J.; Yi, B. A novel non-noble electrocatalyst for PEM fuel cell based on molybdenum nitride. *Electrochem. Commun.* **2006**, *8*, 707−712.
(29) Yuan, Y.; Yang, L.; He, B.; Pervaiz, E.; Shao, Z.; Yang, M. Cobalt−zinc nitride on nitrogen doped carbon black nanohybrids as a non-noble metal electrocatalyst for oxygen reduction reaction. *Nanoscale* **2017**, *9*, 6259−6263.
(30) Xiao, P.; Chen, W.; Wang, X. A Review of Phosphide-Based Materials for Electrocatalytic Hydrogen Evolution. *Adv. Energy Mater.* **2015**, *5*, No. 1500985.
(31) Li, Y.; Dong, Z.; Jiao, L. Multifunctional Transition Metal-Based Phosphides in Energy-Related Electrocatalysis. *Adv. Energy Mater.* **2020**, *10*, No. 1902104.
(32) Mendoza-Garcia, A.; Su, D.; Sun, S. Sea urchin-like cobalt−iron phosphide as an active catalyst for oxygen evolution reaction. *Nanoscale* **2016**, *8*, 3244−3247.
(33) Read, C. G.; Callejas, J. F.; Holder, C. F.; Schaak, R. E. General Strategy for the Synthesis of Transition Metal Phosphide Films for Electrocatalytic Hydrogen and Oxygen Evolution. *ACS Appl. Mater. Interfaces* **2016**, *8*, 12798−12803.
(34) Kim, J.; Roh, C.-W.; Sahoo, S. K.; Yang, S.; Bae, J.; Han, J. W.; Lee, H. Highly Durable Platinum Single-Atom Alloy Catalyst for Electrochemical Reactions. *Adv. Energy Mater.* **2018**, *8*, No. 1701476.
(35) He, F.; Li, K.; Yin, C.; Wang, Y.; Tang, H.; Wu, Z. Single Pd atoms supported by graphitic carbon nitride, a potential oxygen reduction reaction catalyst from theoretical perspective. *Carbon* **2017**, *114*, 619−627.
(36) Zhang, C.; Sha, J.; Fei, H.; Liu, M.; Yazdi, S.; Zhang, J.; Zhong, Q.; Zou, X.; Zhao, N.; Yu, H.; Jiang, Z.; Ringe, E.; Yakobson, B. I.; Dong, J.; Chen, D.; Tour, J. M. Single-Atomic Ruthenium Catalytic Sites on Nitrogen-Doped Graphene for Oxygen Reduction Reaction in Acidic Medium. *ACS Nano* **2017**, *11*, 6930−6941.
(37) Zeng, X.; Shui, J.; Liu, X.; Liu, Q.; Li, Y.; Shang, J.; Zheng, L.; Yu, R. Single-Atom to Single-Atom Grafting of Pt1 onto Fe·N4 Center: Pt1@Fe·N·C Multifunctional Electrocatalyst with Significantly Enhanced Properties. *Adv. Energy Mater.* **2018**, *8*, No. 1701345.
(38) Wang, W.; Jia, Q.; Mukerjee, S.; Chen, S. Recent Insights into the Oxygen-Reduction Electrocatalysis of Fe/N/C Materials. *ACS Catal.* **2019**, *9*, 10126−10141.
(39) Gewirth, A. A.; Varnell, J. A.; DiAscro, A. M. Nonprecious Metal Catalysts for Oxygen Reduction in Heterogeneous Aqueous Systems. *Chem. Rev.* **2018**, *118*, 2313−2339.
(40) Zhao, C.-X.; Li, B.-Q.; Liu, J.-N.; Zhang, Q. Intrinsic Electrocatalytic Activity Regulation of M−N−C Single-Atom Catalysts for the Oxygen Reduction Reaction. *Angew. Chem., Int. Ed.* **2021**, *60*, 4448−4463.
(41) He, Y.; Liu, S.; Priest, C.; Shi, Q.; Wu, G. Atomically dispersed metal−nitrogen−carbon catalysts for fuel cells: advances in catalyst design, electrode performance, and durability improvement. *Chem. Soc. Rev.* **2020**, *49*, 3484−3524.
(42) Sun, T.; Tian, B.; Lu, J.; Su, C. Recent advances in Fe (or Co)/N/C electrocatalysts for the oxygen reduction reaction in polymer electrolyte membrane fuel cells. *J. Mater. Chem.* **2017**, *5*, 18933−18950.
(43) Asset, T.; Atanassov, P. Iron-Nitrogen-Carbon Catalysts for Proton Exchange Membrane Fuel Cells. *Joule* **2020**, *4*, 33−44.
(44) Martinez, U.; Babu, S. K.; Holby, E. F.; Chung, H. T.; Yin, X.; Zelenay, P. Progress in the Development of Fe-Based PGM-Free Electrocatalysts for the Oxygen Reduction Reaction. *Adv. Mater.* **2019**, *31*, No. 1806545.
(45) Chang, C. J.; Loh, Z.-H.; Shi, C.; Anson, F. C.; Nocera, D. G. Targeted Proton Delivery in the Catalyzed Reduction of Oxygen to Water by Bimetallic Pacman Porphyrins. *J. Am. Chem. Soc.* **2004**, *126*, 10013−10020.
(46) McGuire, R., Jr.; Dogutan, D. K.; Teets, T. S.; Suntivich, J.; Shao-Horn, Y.; Nocera, D. G. Oxygen reduction reactivity of cobalt(II) hangman porphyrins. *Chem. Sci.* **2010**, *1*, 411−414.
(47) Carver, C. T.; Matson, B. D.; Mayer, J. M. Electrocatalytic Oxygen Reduction by Iron Tetra-arylporphyrins Bearing Pendant Proton Relays. *J. Am. Chem. Soc.* **2012**, *134*, 5444−5447.
(48) Matson, B. D.; Carver, C. T.; Von Ruden, A.; Yang, J. Y.; Raugei, S.; Mayer, J. M. Distant protonated pyridine groups in water-soluble iron porphyrin electrocatalysts promote selective oxygen reduction to water. *Chem. Commun.* **2012**, *48*, 11100−11102.
(49) Samanta, S.; Mittra, K.; Sengupta, K.; Chatterjee, S.; Dey, A. Second Sphere Control of Redox Catalysis: Selective Reduction of O_2 to O_2^- or H_2O by an Iron Porphyrin Catalyst. *Inorg. Chem.* **2013**, *52*, 1443−1453.
(50) Ghatak, A.; Samanta, S.; Nayek, A.; Mukherjee, S.; Dey, S. G.; Dey, A. Second-Sphere Hydrogen-Bond Donors and Acceptors Affect the Rate and Selectivity of Electrochemical Oxygen Reduction by Iron Porphyrins Differently. *Inorg. Chem.* **2022**, *61*, 12931−12947.
(51) Singha, A.; Mondal, A.; Nayek, A.; Dey, S. G.; Dey, A. Oxygen Reduction by Iron Porphyrins with Covalently Attached Pendent Phenol and Quinol. *J. Am. Chem. Soc.* **2020**, *142*, 21810−21828.
(52) Collman, J. P.; Denisevich, P.; Konai, Y.; Marrocco, M.; Koval, C.; Anson, F. C. Electrode catalysis of the four-electron reduction of oxygen to water by dicobalt face-to-face porphyrins. *J. Am. Chem. Soc.* **1980**, *102*, 6027−6036.
(53) Song, E.; Shi, C.; Anson, F. C. Comparison of the Behavior of Several Cobalt Porphyrins as Electrocatalysts for the Reduction of O_2 at Graphite Electrodes. *Langmuir* **1998**, *14*, 4315−4321.
(54) Shi, C.; Anson, F. C. (5,10,15,20-Tetramethylporphyrinato)-cobalt(II): A Remarkably Active Catalyst for the Electroreduction of O_2 to H_2O. *Inorg. Chem.* **1998**, *37*, 1037−1043.
(55) Sinha, S.; Ghosh, M.; Warren, J. J. Changing the Selectivity of O_2 Reduction Catalysis with One Ligand Heteroatom. *ACS Catal.* **2019**, *9*, 2685−2691.
(56) Fukushima, T.; Drisdell, W.; Yano, J.; Surendranath, Y. Graphite-Conjugated Pyrazines as Molecularly Tunable Heterogeneous Electrocatalysts. *J. Am. Chem. Soc.* **2015**, *137*, 10926−10929.
(57) Braley, S. E.; Xie, J.; Losovyj, Y.; Smith, J. M. Graphite Conjugation of a Macrocyclic Cobalt Complex Enhances Nitrite Electroreduction to Ammonia. *J. Am. Chem. Soc.* **2021**, *143*, 7203−7208.
(58) Ghosh, M.; Braley, S. E.; Ezhov, R.; Worster, H.; Valdez-Moreira, J. A.; Losovyj, Y.; Jakubikova, E.; Pushkar, Y. N.; Smith, J. M. A Spectroscopically Observed Iron Nitrosyl Intermediate in the Reduction of Nitrate by a Surface-Conjugated Electrocatalyst. *J. Am. Chem. Soc.* **2022**, *144*, 17824−17831.
(59) Sun, Q.; Wang, Q.; Li, F.; Liu, Y.; Li, X.; Zhu, Z.; Chen, J.; Peng, Y.-K.; Gu, J. Carbon-Conjugated Co Complexes as Model Electrocatalysts for Oxygen Reduction Reaction. *Catalysts* **2023**, *13*, No. 330.
(60) Zhou, Y.; Lu, R.; Tao, X.; Qiu, Z.; Chen, G.; Yang, J.; Zhao, Y.; Feng, X.; Müllen, K. Boosting Oxygen Electrocatalytic Activity of Fe−N−C Catalysts by Phosphorus Incorporation. *J. Am. Chem. Soc.* **2023**, *145*, 3647−3655.
(61) Welsh, W. A.; Reynolds, G. J.; Henry, P. M. Synthesis of hydroxy-substituted macrocyclic ligand complexes of cobalt and isolation of a macrocycle precursor. *Inorg. Chem.* **1977**, *16*, 2558−2561.
(62) Jackels, S. C.; Farmery, K.; Barefield, E. K.; Rose, N. J.; Busch, D. H. Tetragonal cobalt(III) complexes containing tetradentate macrocyclic amine ligands with different degrees of unsaturation. *Inorg. Chem.* **1972**, *11*, 2893−2901.
(63) Oh, S.; Gallagher, J. R.; Miller, J. T.; Surendranath, Y. Graphite-Conjugated Rhenium Catalysts for Carbon Dioxide Reduction. *J. Am. Chem. Soc.* **2016**, *138*, 1820−1823.
(64) Ravel, B.; Newville, M. ATHENA, ARTEMIS, HEPHAESTUS: data analysis for X-ray absorption spectroscopy using IFEFFIT. *J. Synchrotron Radiat.* **2005**, *12*, 537−541.
(65) Rehr, J. J.; Albers, R. C. Theoretical approaches to x-ray absorption fine structure. *Rev. Mod. Phys.* **2000**, *72*, No. 621.

https://doi.org/10.1021/acsaem.4c01216
ACS Appl. Energy Mater. 2024, 7, 6717−6726

(66) Gao, M.; Sheng, W.; Zhuang, Z.; Fang, Q.; Gu, S.; Jiang, J.; Yan, Y. Efficient Water Oxidation Using Nanostructured α-Nickel-Hydroxide as an Electrocatalyst. *J. Am. Chem. Soc.* **2014**, *136*, 7077−7084.
(67) Gojković, S. L.; Gupta, S.; Savinell, R. F. Heat-treated iron(III) tetramethoxyphenyl porphyrin chloride supported on high-area carbon as an electrocatalyst for oxygen reduction: Part II. Kinetics of oxygen reduction. *J. Electroanal. Chem.* **1999**, *462*, 63−72.
(68) Paulus, U. A.; Schmidt, T. J.; Gasteiger, H. A.; Behm, R. J. Oxygen reduction on a high-surface area Pt/Vulcan carbon catalyst: a thin-film rotating ring-disk electrode study. *J. Electroanal. Chem.* **2001**, *495*, 134−145.
(69) Bard, A. J. F.; Larry, R. *Electrochemical Methods: Fundamentals and Applications*; J. Wiley and Sons: New York, 2000.
(70) Zhang, R.; Warren, J. J. Controlling the Oxygen Reduction Selectivity of Asymmetric Cobalt Porphyrins by Using Local Electrostatic Interactions. *J. Am. Chem. Soc.* **2020**, *142*, 13426−13434.
(71) Wagner, C. D. *The NIST X-Ray Photoelectron Spectroscopy (XPS) Database*; CiNii: Washington, D.C., 1991.
(72) Ding, R.; Qi, L.; Jia, M.; Wang, H. Facile and large-scale chemical synthesis of highly porous secondary submicron/micron-sized $NiCo_2O_4$ materials for high-performance aqueous hybrid AC-$NiCo_2O_4$ electrochemical capacitors. *Electrochim. Acta* **2013**, *107*, 494−502.
(73) Seifullina, I. I.; Skorokhod, L. S.; Pulya, A. V.; Vlasenko, V. G.; Trigub, A. L.; Rakipow, I. M. Synthesis, Structure, and Properties of Co^{2+} and Ni^{2+} Complexes with the Product of Condensation of 2-(7-Bromo-2-oxo-5-phenyl-3H-1,4-benzodiazepin-1-yl)acetohydrazide and 1H-Indole-2,3-dione. *Russ. J. Gen. Chem.* **2020**, *90*, 1298−1303.
(74) Hachmöller, O.; Buzanich, A. G.; Aichler, M.; Radtke, M.; Dietrich, D.; Schwamborn, K.; Lutz, L.; Werner, M.; Sperling, M.; Walch, A.; Karst, U. Elemental bioimaging and speciation analysis for the investigation of Wilson's disease using μXRF and XANES. *Metallomics* **2016**, *8*, 648−653.
(75) Faggi, E.; Gavara, R.; Bolte, M.; Fajarí, L.; Juliá, L.; Rodríguez, L.; Alfonso, I. Copper(II) complexes of macrocyclic and open-chain pseudopeptidic ligands: synthesis, characterization and interaction with dicarboxylates. *Dalton Trans.* **2015**, *44*, 12700−12710.
(76) Owen, M. E.; Carter, E.; Hutchings, G. J.; Ward, B. D.; Murphy, D. M. Influence of counterions on the structure of bis(oxazoline)-copper(II) complexes; an EPR and ENDOR investigation. *Dalton Trans.* **2012**, *41*, 11085−11092.
(77) Ezhov, R.; Maximova, O.; Lyu, X.; Leshchev, D.; Stavitski, E.; Serov, A.; Pushkar, Y. Spectroscopic Characterization of Highly Active Fe−N−C Oxygen Reduction Catalysts and Discovery of Strong Interaction with Nafion Ionomer. *ACS Appl. Energy Mater.* **2024**, *7*, 604−613.
(78) Sinha, S.; Mirica, L. M. Electrocatalytic O_2 Reduction by an Organometallic Pd(III) Complex via a Binuclear Pd(III) Intermediate. *ACS Catal.* **2021**, *11*, 5202−5211.
(79) Adžić, R. R.; Wang, J. X. Configuration and Site of O_2 Adsorption on the Pt(111) Electrode Surface. *J. Phys. Chem. B* **1998**, *102*, 8988−8993.
(80) Freakley, S. J.; He, Q.; Harrhy, J. H.; Lu, L.; Crole, D. A.; Morgan, D. J.; Ntainjua, E. N.; Edwards, J. K.; Carley, A. F.; Borisevich, A. Y.; Kiely, C. J.; Hutchings, G. J. Palladium-tin catalysts for the direct synthesis of H_2O_2 with high selectivity. *Science* **2016**, *351*, 965−968.
(81) Campos-Martin, J. M.; Blanco-Brieva, G.; Fierro, J. L. G. Hydrogen Peroxide Synthesis: An Outlook beyond the Anthraquinone Process. *Angew. Chem., Int. Ed.* **2006**, *45*, 6962−6984.
(82) Edwards, J. K.; Solsona, B.; N, E. N.; Carley, A. F.; Herzing, A. A.; Kiely, C. J.; Hutchings, G. J. Switching Off Hydrogen Peroxide Hydrogenation in the Direct Synthesis Process. *Science* **2009**, *323*, 1037−1041.
(83) Sun, Y.; Silvioli, L.; Sahraie, N. R.; Ju, W.; Li, J.; Zitolo, A.; Li, S.; Bagger, A.; Arnarson, L.; Wang, X.; Moeller, T.; Bernsmeier, D.; Rossmeisl, J.; Jaouen, F.; Strasser, P. Activity−Selectivity Trends in the Electrochemical Production of Hydrogen Peroxide over Single-Site Metal−Nitrogen−Carbon Catalysts. *J. Am. Chem. Soc.* **2019**, *141*, 12372−12381.
(84) Alvarado-Leal, L. A.; Paez-Ornelas, J. I.; Fernández-Escamilla, H. N.; Perez-Tijerina, E. G.; Guerrero-Sánchez, J.; Romo-Herrera, J. M.; Takeuchi, N. Influence of the Atomic Local Environment on the ORR Activity of Single-Atom Catalysts in N-Doped Graphene. *ACS Appl. Energy Mater.* **2024**, *7*, 4794−4802.
(85) Yu, M.; Li, A.; Kan, E.; Zhan, C. Substantial Impact of Spin State Evolution in OER/ORR Catalyzed by Fe−N−C. *ACS Catal.* **2024**, *14*, 6816−6826.
(86) Chen, G.; Zhong, H.; Feng, X. Active site engineering of single-atom carbonaceous electrocatalysts for the oxygen reduction reaction. *Chem. Sci.* **2021**, *12*, 15802−15820.
(87) Ghatak, A.; Bhakta, S.; Bhunia, S.; Dey, A. Influence of the distal guanidine group on the rate and selectivity of O_2 reduction by iron porphyrin. *Chem. Sci.* **2019**, *10*, 9692−9698.
(88) Bhunia, S.; Rana, A.; Roy, P.; Martin, D. J.; Pegis, M. L.; Roy, B.; Dey, A. Rational Design of Mononuclear Iron Porphyrins for Facile and Selective $4e^-/4H^+$ O_2 Reduction: Activation of O−O Bond by 2nd Sphere Hydrogen Bonding. *J. Am. Chem. Soc.* **2018**, *140*, 9444−9457.
(89) Dunwell, M.; Luc, W.; Yan, Y.; Jiao, F.; Xu, B. Understanding Surface-Mediated Electrochemical Reactions: CO_2 Reduction and Beyond. *ACS Catal.* **2018**, *8*, 8121−8129.
(90) Fang, Y.-H.; Liu, Z.-P. Tafel Kinetics of Electrocatalytic Reactions: From Experiment to First-Principles. *ACS Catal.* **2014**, *4*, 4364−4376.
(91) Limaye, A. M.; Zeng, J. S.; Willard, A. P.; Manthiram, K. Bayesian data analysis reveals no preference for cardinal Tafel slopes in CO_2 reduction electrocatalysis. *Nat. Commun.* **2021**, *12*, No. 703.

https://doi.org/10.1021/acsaem.4c01216
ACS Appl. Energy Mater. 2024, 7, 6717−6726